

Supporting Information for:

A Metal-Organic Framework with Dual Fluorescent Emission Based on 3-Aminoisonicotinate: Luminescence Thermometry and Fe³⁺ Sensing in Hybrid Membranes

Oier Pajuelo-Corral,^{*a} Eneko Alkain,^b Ricardo F. Mendes,^c Filipe A. Almeida Paz,^c Antonio Rodríguez-Diéguez,^d Jose Angel García,^e Jose Manuel Seco^b and Javier Cepeda ^{*b}

^a POLYMAT, Universidad del País Vasco/Euskal Herriko Unibertsitatea (UPV/EHU), Facultad de Química, 20018 Donostia-San Sebastian, Spain. ^b Departamento de Química Aplicada, Facultad de Química, Universidad del País Vasco/Euskal Herriko Unibertsitatea (UPV/EHU), 20018 Donostia-San Sebastian, Spain. ^c Department of Chemistry, CICECO-Aveiro Institute of Materials, University of Aveiro, 3810-193 Aveiro, Portugal. ^e Departamento de Química Inorgánica, Facultad de Ciencias, Universidad de Granada, Av. Fuentenueva S/N, 18071 Granada, Spain. ^e Departamento de Física, Facultad de Ciencia y Tecnología, Universidad del País Vasco/Euskal Herriko Unibertsitatea (UPV/EHU), 48940, Leioa, Spain.

Contents:

- S1. Experimental details.
- S2. Chemical characterization of compounds.
- S3. FT-IR spectroscopy.
- S4. Powder X-ray diffraction analysis.
- S5. Continuous Shape Measurements.
- S6. Structural details
- S7. Photoluminescence measurements.
- S8. Lifetime measurements.
- S9. DFT calculations.
- S10. Thermometric analysis.
- S11. Vacuum- and temperature-induced PL in membranes.
- S12. Sensing in membranes.
- S13. Scanning electron microscopy.
- S14. References.

S1. Experimental details.

Chemical characterization. Elemental analyses (C, H, N) were performed on a Leco CHNS-932 microanalyzer. IR spectra were recorded using KBr pellets in a ThermoNicolet IR 200 spectrometer in the 4000–400 cm^{-1} region. Diffuse reflectance measurements were performed on a UV-2600 UV/vis Shimadzu spectrophotometer using BaSO_4 as reference material. Thermal analyses (TG/DTA) were performed using a TA SDT 2960 thermal analyzer in a synthetic air atmosphere (79% N_2 / 21% O_2) with a 5 $^\circ\text{C}\cdot\text{min}^{-1}$ heating rate.

X-ray Diffraction Data Collection and Structure Determination. Suitable single crystals of **1** were used for the structure determination. Single crystal X-ray diffraction (SCXD) data collection was done at 100(2) K on a Bruker VENTURE area detector equipped with graphite monochromated $\text{Mo K}\alpha$ radiation ($\lambda = 0.71073 \text{ \AA}$) by applying the ω -scan method. Data reduction was performed with the APEX2¹ software and corrected for absorption using SADABS² Crystal structures were solved by direct methods using the SHELX program³ and refined by full-matrix least-squares on F^2 including all reflections employing the Olex2 software.⁴ All hydrogen atoms were located in the difference Fourier map and included as fixed contributions using riding models with isotropic thermal displacement parameters 1.2 times those of their parent atoms for the 3isoani ligand. Crystallographic data has been deposited with the Cambridge Crystallographic Data Center as supplementary publication with nos. CCDC 2412031. Copies of the data can be obtained free of charge on application to the Director, CCDC, 12 Union Road, Cambridge, CB2 1EZ, U.K. (Fax: +44-1223-335033; e-mail: deposit@ccdc.cam.ac.uk or <http://www.ccdc.cam.ac.uk>).

The powder X-ray diffraction (PXRD) patterns were measured over polycrystalline samples. For data acquisition, a Philips X'PERT powder diffractometer was used with $\text{Cu-K}\alpha$ radiation ($\lambda = 1.5418 \text{ \AA}$) over the $5 < 2\theta < 50^\circ$ range with a step size of 0.026° and an acquisition time of 2.5 s per step at 25 $^\circ\text{C}$. Indexation of diffraction profiles was made using the FULLPROF program (pattern matching analysis)⁵ based on the space group and cell parameters obtained from single crystal X-ray diffraction.

Photoluminescence measurements. Photoluminescent measurements in the 10-310 K range were recorded under high vacuum (of ca. 10^{-9} mbar) in order to avoid the presence of oxygen or water in the sample holder in a closed-cycle helium cryostat enclosed in an Edinburgh Instruments FLS920 spectrometer using polycrystalline samples. For steady-state measurements, an IK3552r-G HeCd continuous laser (325 nm) and a Müller-Elektronik-Optik SVX1450 Xe lamp were used as excitation sources. In contrast, a pulsed laser diode was employed for the lifetimes measurements. Photographs of the irradiated single-crystals were taken at room temperature in a micro-PL system included in an Olympus optical microscope illuminated with an HeCd laser or an Hg lamp. Quantum Yield measurements were performed using polycrystalline samples in a Horiba Quante-f integrating sphere using an Oriel Instruments MS257 lamp as

an excitation source and iHR550 spectrometer from Horiba to analyze the emission.

Computational details. TD-DFT calculations were performed over a suitable model of compound **1** obtained from single-crystal X-ray measurements using the Gaussian 09 package.⁶ The Becke three-parameter hybrid functional with the nonlocal correlation functional of Lee-Yang-Parr (B3LYP)⁷⁻⁹ and 6-311G(d) basis for non-metallic atoms and the LANL2DZ basis set for Zn(II) was employed.¹⁰⁻¹² The results were analysed with the GausSum programme¹³ and the molecular orbitals were plotted using the GaussView software.¹⁴

S2. Chemical characterization of compounds.

The thermogravimetric analysis shown in Fig. S1 corresponds to a fresh sample of the material (recently filtered from the mother liquors). The TG curve shows a faint mass loss from room temperature to 300 °C which could be attributed to the lattice water molecules. Nonetheless, the mass loss does not account for the total number of water molecules foreseen by single-crystal X-ray measurements. Probably, the low interaction with the framework makes them prone to be released from the pores of the framework, for which the liberation of part of the molecules was already produced during the stabilization process. Then, the degradation of 3isoani occurs in the 300-450 °C temperature range and the subsequent formation of ZnO as the final residue.

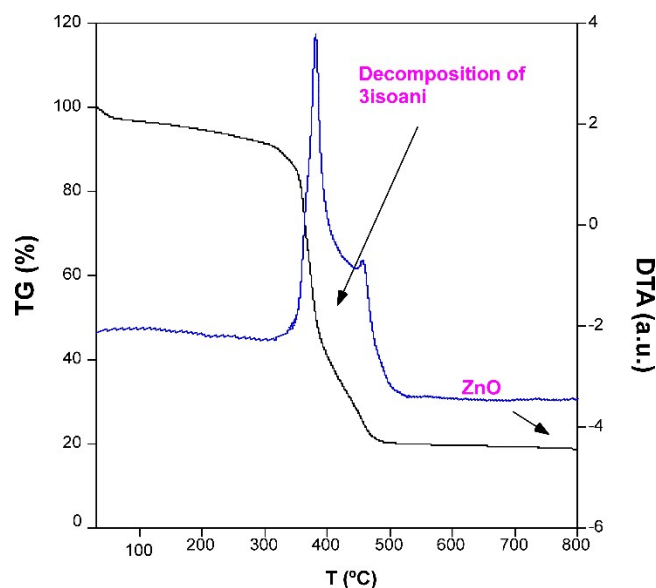


Figure S1. TG/DTA curves of compound 1.

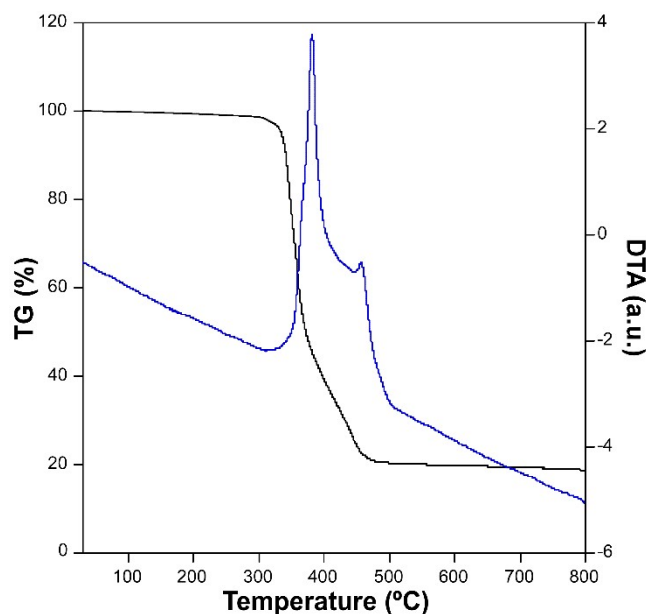


Figure S2. TG/DTA curves of the dehydrated compound 1 after the thermal treatment at 50 °C for 3 h.

S3. FT-IR spectroscopy

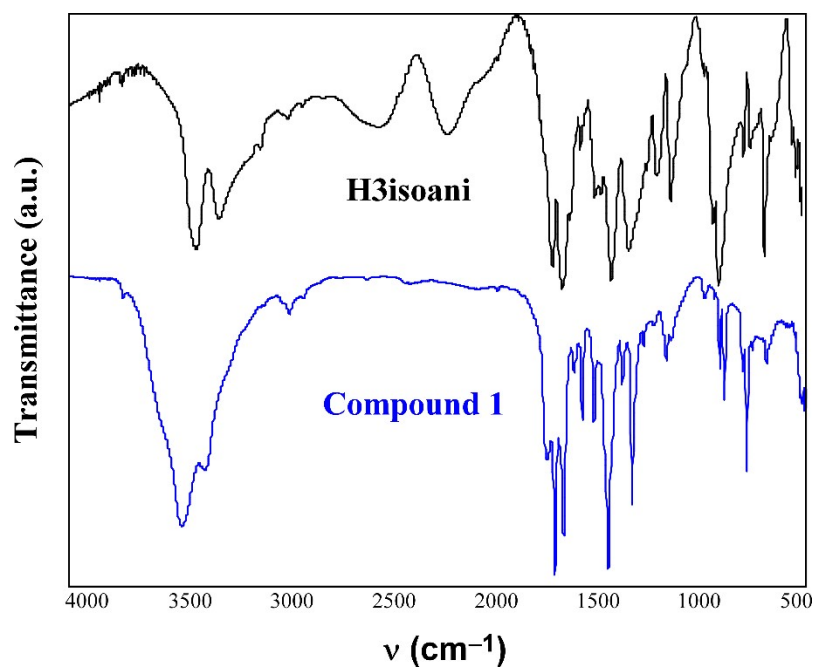


Figure S3. FT-IR spectra of H3isoani and compound 1.

S4. Powder X-ray diffraction analysis.

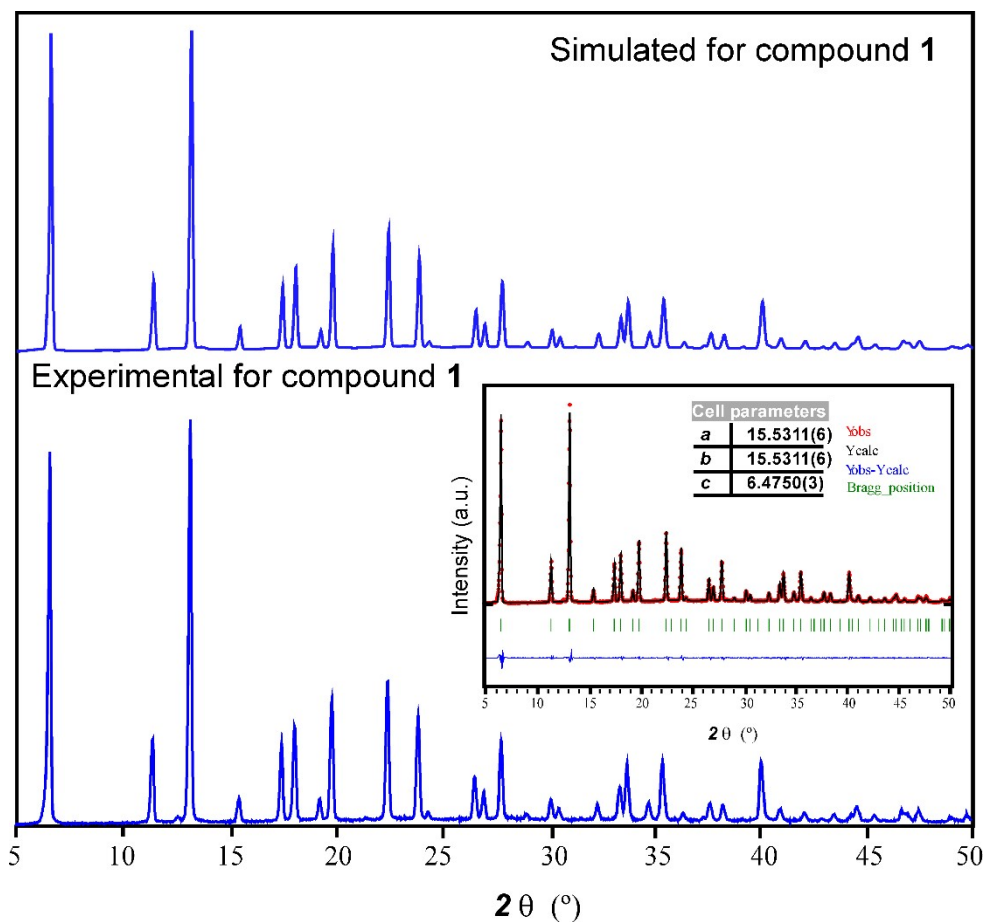


Figure S4. Comparison between the experimental PXRD data for compound **1** with that simulated from the crystal structure of **1**. Inset represents the pattern-matching analysis.

S5. Continuous Shape Measurements

Table S1. CShMs for the tetrahedral coordination environment for compound **1**. The lowest SHAPE value is highlighted indicating the best result. Codes:

SP-4	1 D4h	Square
T-4	2 Td	Tetrahedron
SS-4	3 C2v	Seesaw
vTBPY-4	4 C3v	Vacant trigonal bipyramid

Structure [ML4]	SP-4	T-4	SS-4	vTBPY-4
Compound 1	24.944	1.068	6.922	3.717

S6. Structural details.

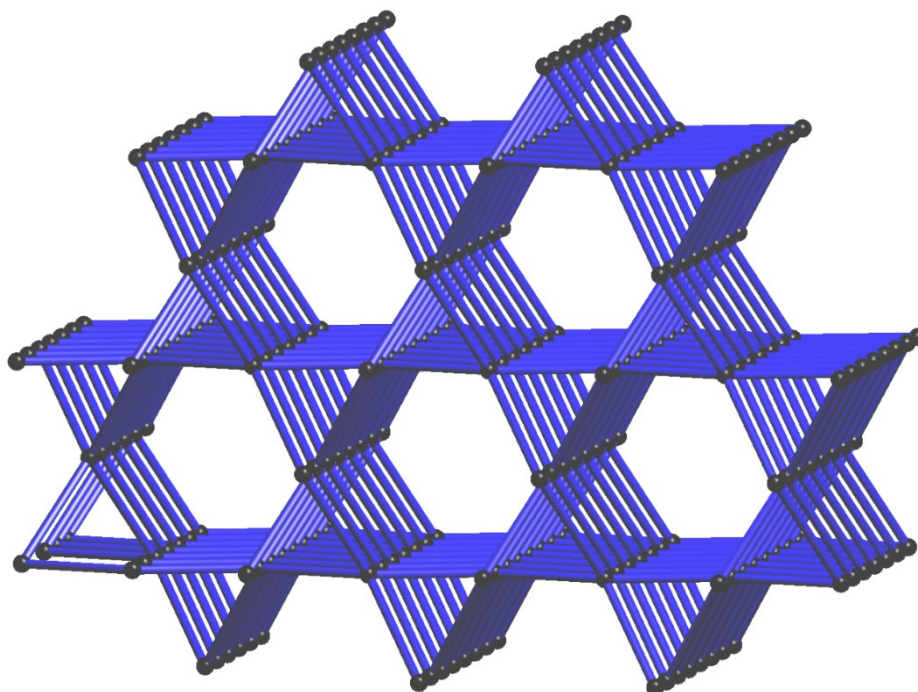


Figure S5. Schematic view of the simplified **qtz** network topology of compound **1**.

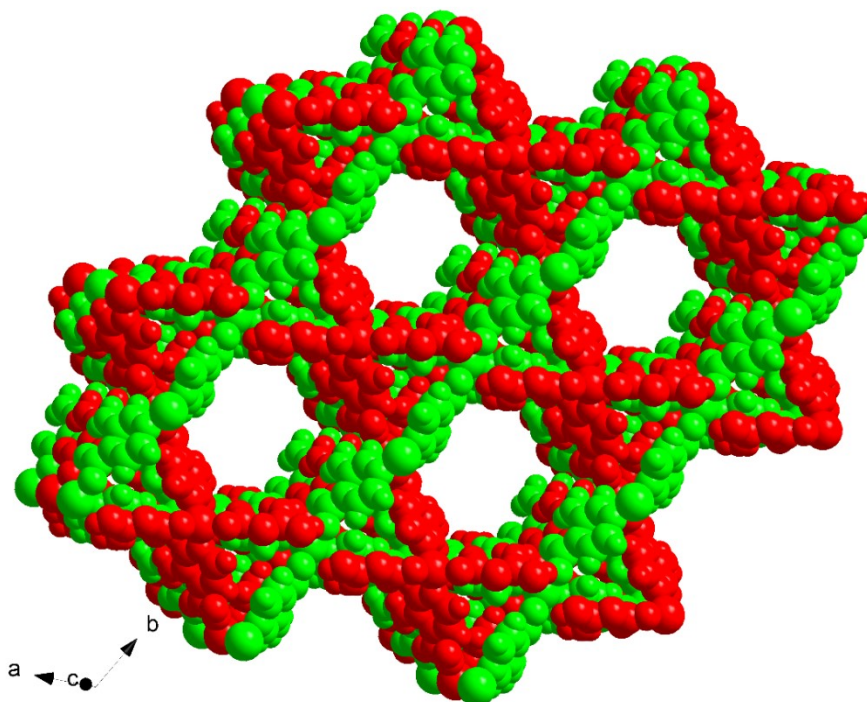


Figure S6. Illustration of the interpenetrated nature of compound **1** where each colour represents a subnetwork. Lattice water molecules have been omitted for clarity.

Table S2. Selected bond lengths (Å) for compound **1**.¹

Compound 1			
Zn1-O1	1.973(6)	Zn1-N1(i)	2.018(6)
Zn1-O3(i)	1.928(5)	Zn1-N2(ii)	2.062(7)

¹Symmetry codes: (i) -y, x-y, -2/3+z; (ii) 1-y, x-y, -2/3+z.

Table S3. Selected bond angles for compound **1** (°).¹

O1 Zn1 N1(i)	102.2(2)	O3 Zn1 N1(i)	123.1(2)
O1 Zn1 N2(ii)	119.1(3)	O3 Zn1 N2(ii)	101.9(2)
O3 Zn1 O1	101.7(2)	N1(i) Zn1 N2(ii)	109.7(3)

¹Symmetry codes: (i) -y, x-y, -2/3+z; (ii) 1-y, x-y, -2/3+z.

Table S4. Structural parameters (Å, °) of hydrogen bonds in compound **1**.

<i>D-H</i> ... <i>A</i>	<i>D-H</i>	<i>H</i> ... <i>A</i>	<i>D</i> ... <i>A</i>	<i>D-H</i> ... <i>A</i>
N31-H31B...O2	0.88	2.21	2.722(4)	116.24

^a D: donor. A: acceptor.

S7. Photoluminescence measurements.

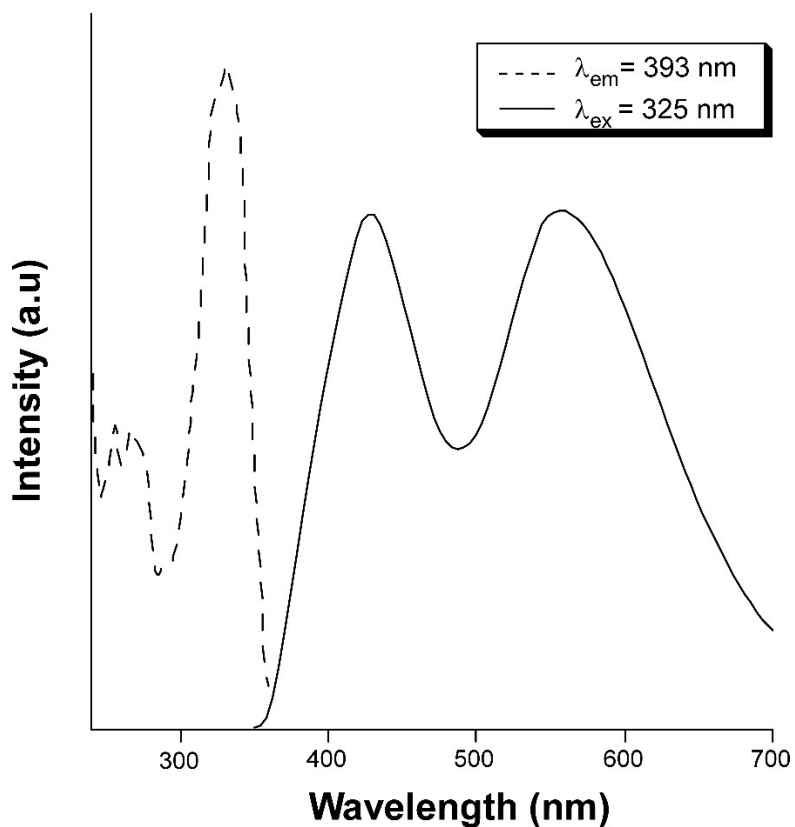


Figure S7. Excitation and emission spectra H3isoani recorded at room temperature.

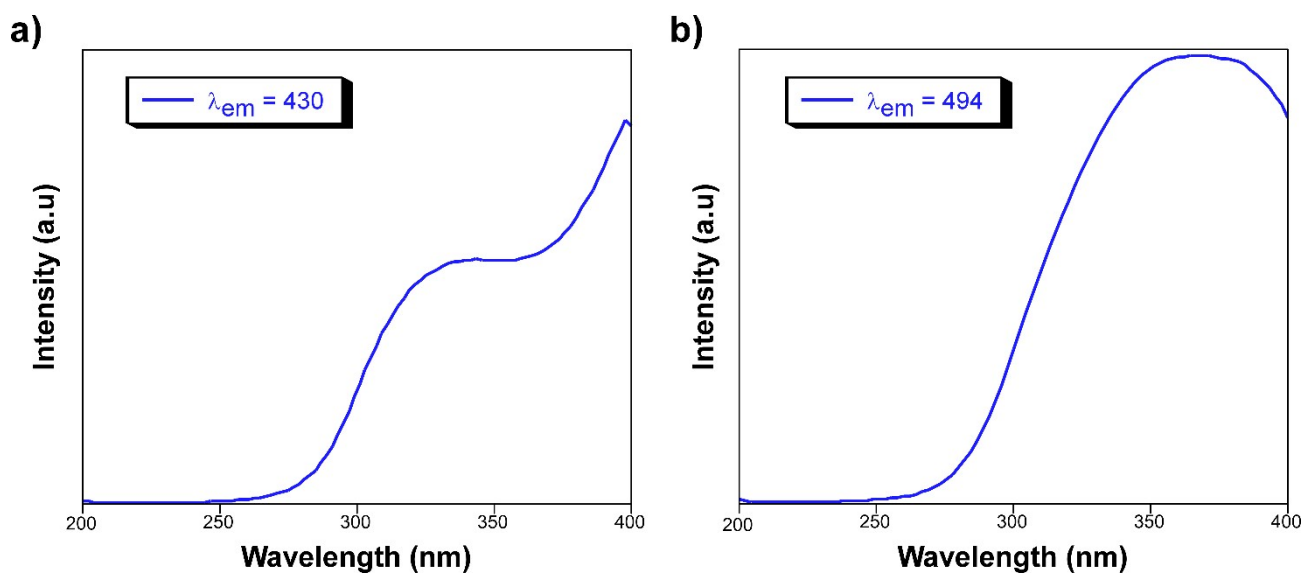


Figure S8. Excitation spectra at room temperature of compound 1 recorded at an emission wavelength of a) 430 nm and b) 494 nm.

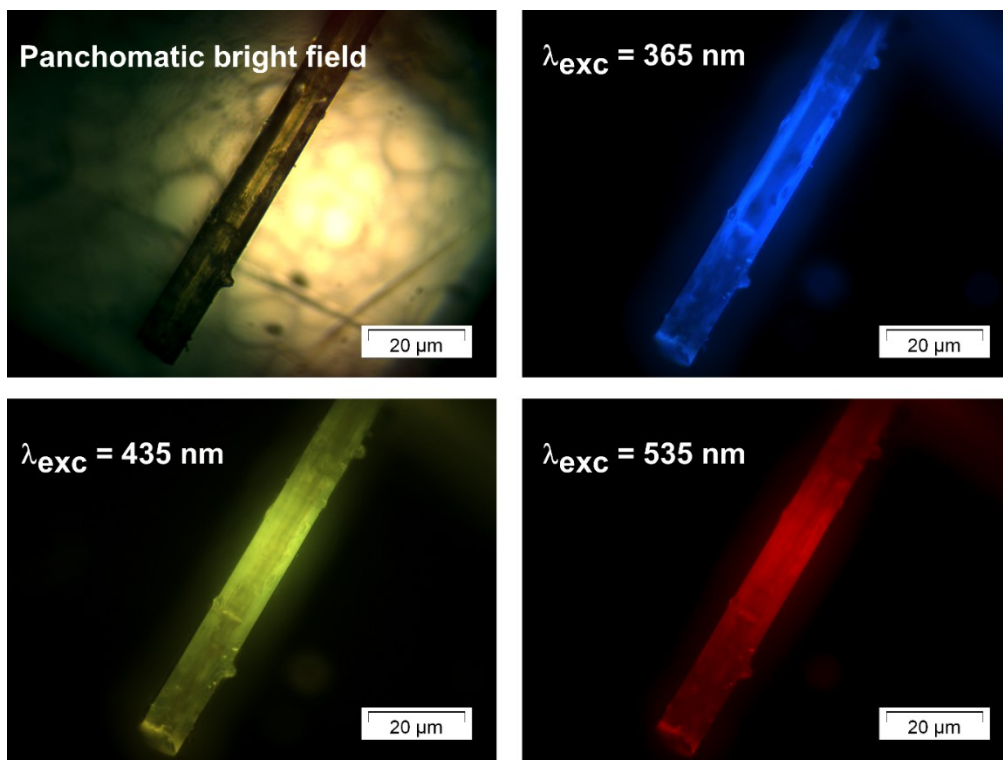


Figure S9. Micro-PL images taken on single-crystal of **1** under panchromatic field at different excitation wavelengths.

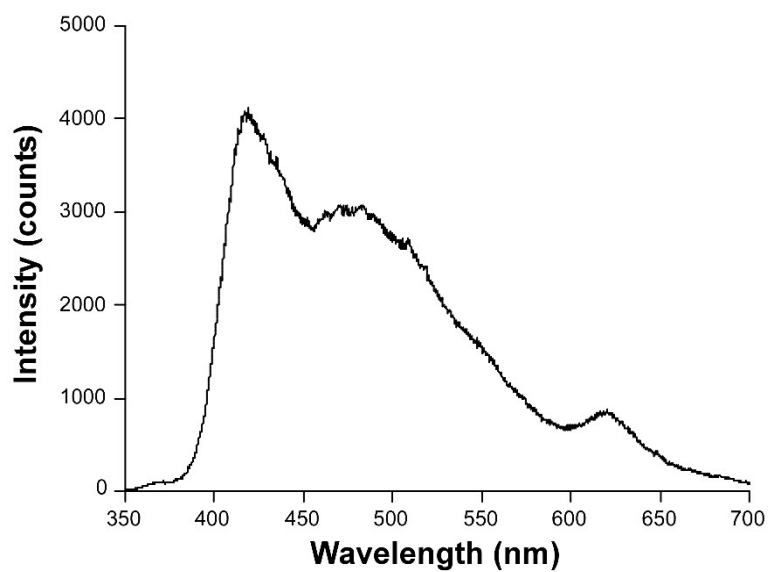


Figure S10. Emission spectrum of compound **1** at room temperature ($\lambda_{\text{ex}} = 255 \text{ nm}$).

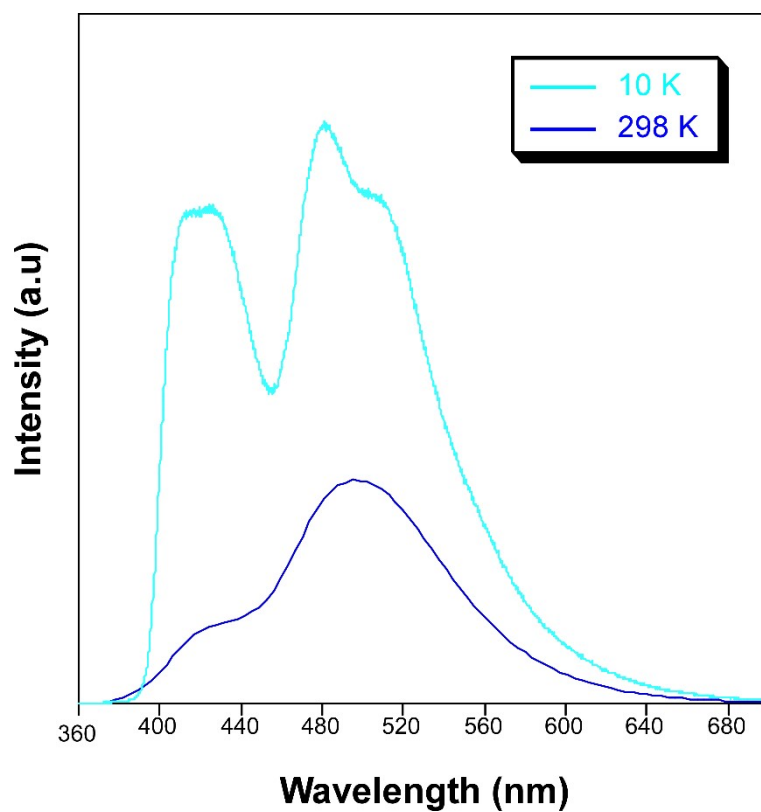


Figure S11. Comparison between emission spectra of compound **1** at room temperature and 10 K ($\lambda_{\text{ex}} = 325$ nm).

S8. Lifetime measurements.

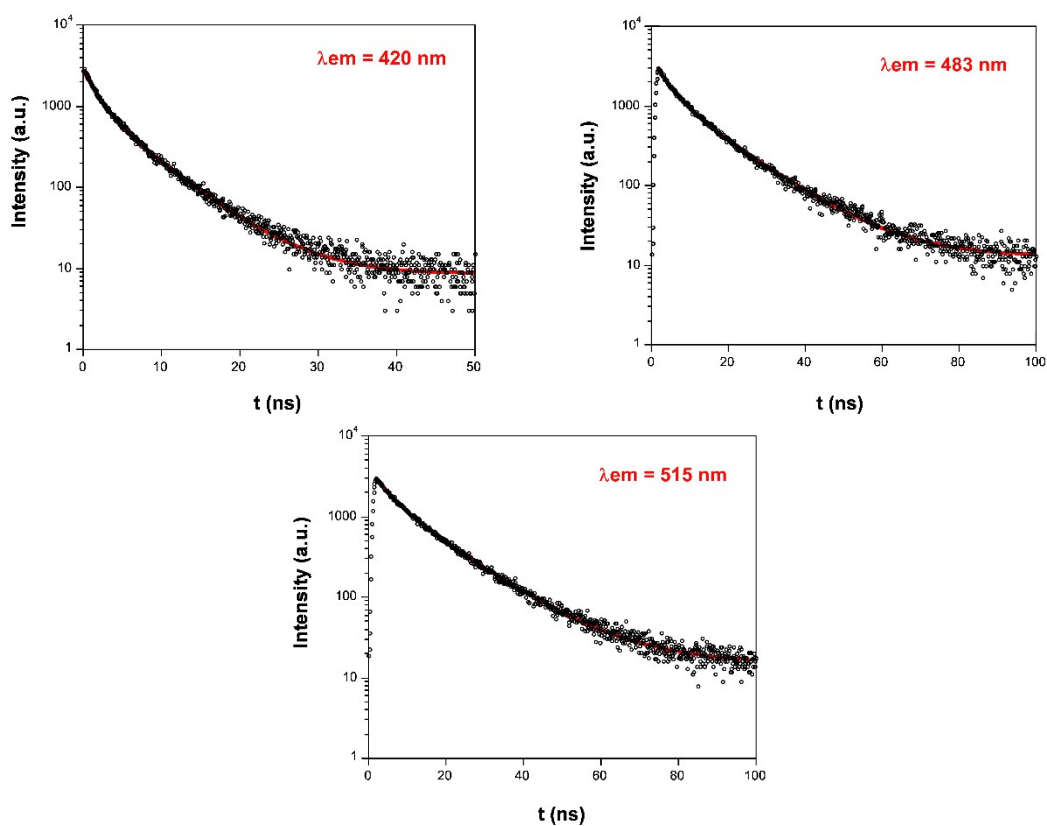


Figure S12. Recorded emission decay curves at 10 K at selected emission wavelength showing the best fitting for **1** ($\lambda_{\text{ex}} = 325$ nm).

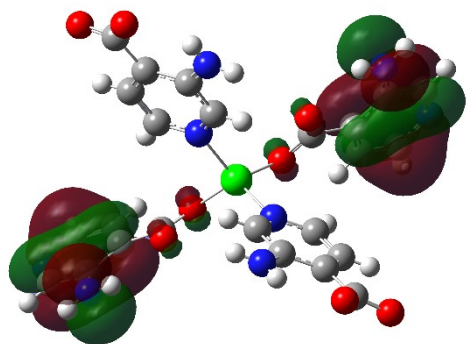
Table S5. The best fit results of decay curves were performed at 10 K for compound **1** and monitored at different emission wavelengths.

Wavelength (nm)	τ_1 (ns)	τ_2 (ns)	$\langle \tau_{\text{av}} \rangle$ (ns)	Chi Sq.
420	1.70(2) / 31.5%	5.87(3) / 68.5%	4.54	1.198
483	4.04(5) / 24.7%	13.14(6) / 75.3%	10.87	1.146
515	5.03(8) / 23.3%	13.91(8) / 76.7%	11.87	0.994

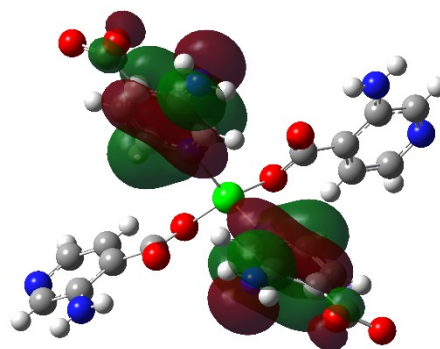
S9. DFT calculations.

Table S6. Experimental and calculated main excitation wavelengths (nm) at 10 K. Singlet electronic transitions and associated oscillator strengths were calculated on model **1** in gas phase.

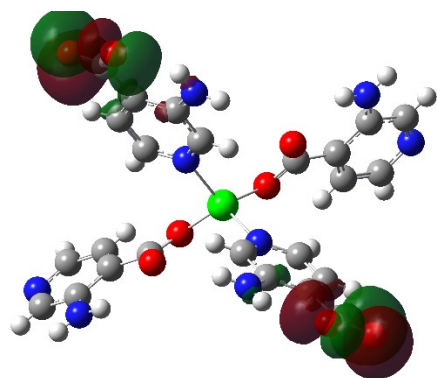
Exp. λ	Calc. λ	Significant contributions	State	Osc. st. (a.u.)
255	277	HOMO - 7 \rightarrow LUMO + 3 (36%) HOMO - 2 \rightarrow LUMO + 6 (30%)	49	0.1405
	282	HOMO - 8 \rightarrow LUMO (54%) HOMO - 9 \rightarrow LUMO + 1 (38%)	45	0.2319
365	362	HOMO - 2 \rightarrow LUMO + 2 (57%) HOMO - 3 \rightarrow LUMO + 3 (42%)	19	0.0296



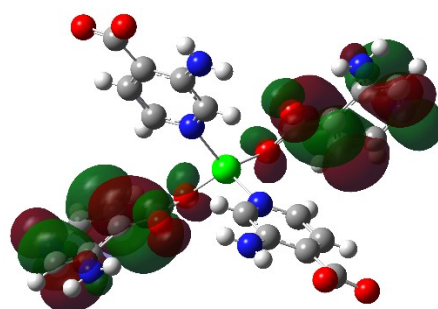
HOMO-7



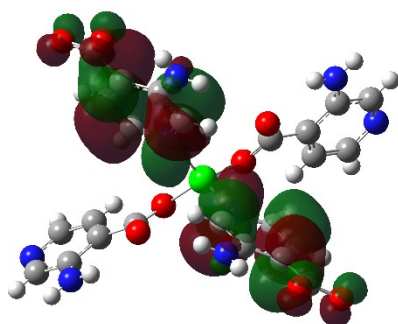
HOMO-6



HOMO-2



LUMO



LUMO+3

S10. Thermometric analysis.

The thermometric analysis was initially conducted for the low temperature region (10–310 K). In view of the structured shape of the two main bands of the emission spectrum of compound **1**, the spectra have been first converted to energy units (eV) and then properly decomposed by fitting the bands according to gaussian functions. Faithful fittings have been achieved by using four functions (two functions per main band) for the low temperature region (10–200 K) whereas the spectra were better reproduced with only three gaussian functions (two for the low-energy band and one for the high-energy band) for the high temperature region (210–310 K). The ratiometric analysis was then performed in terms of the integrated intensity provided by each band (summing the corresponding areas of the gaussian functions).

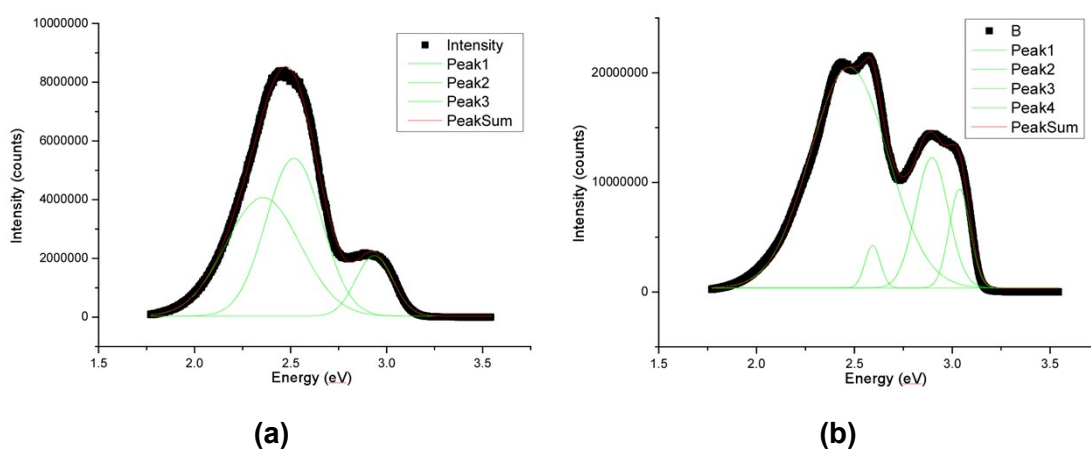


Figure S13. Decomposition of the emission spectra into several gaussian functions at: (a) 310 K and (b) 10 K.

The high-temperature region was analyzed with the same methodology, using 3 components for fitting all the inspected temperatures in the 310–520 K range. As observed below, the evolution of the emission pattern is progressive with the temperature and does not characterize for significant sensitivity.

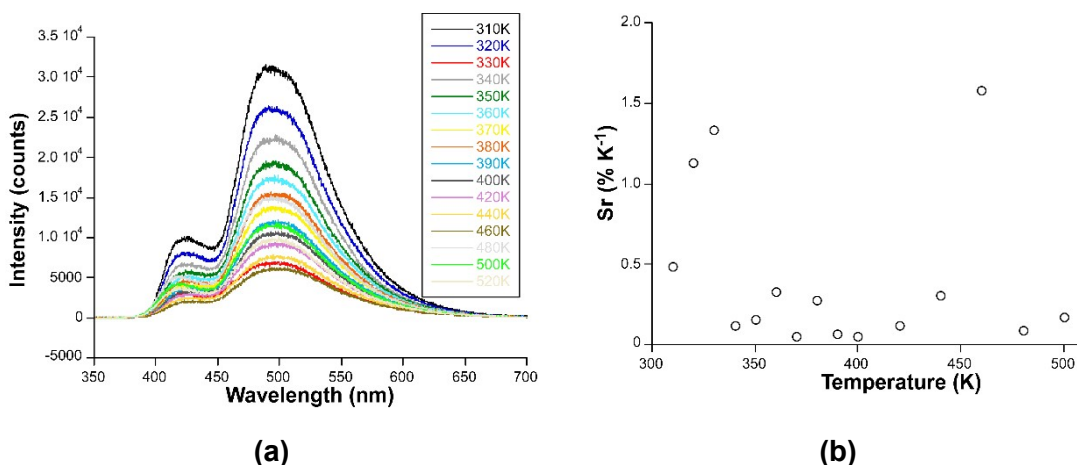


Figure S14. Thermometric activity of compound **1** in the high-temperature range showing (a) the evolution of the emission spectra and (b) the relative sensitivity.

S11. Vacuum- and temperature-induced PL in membranes.

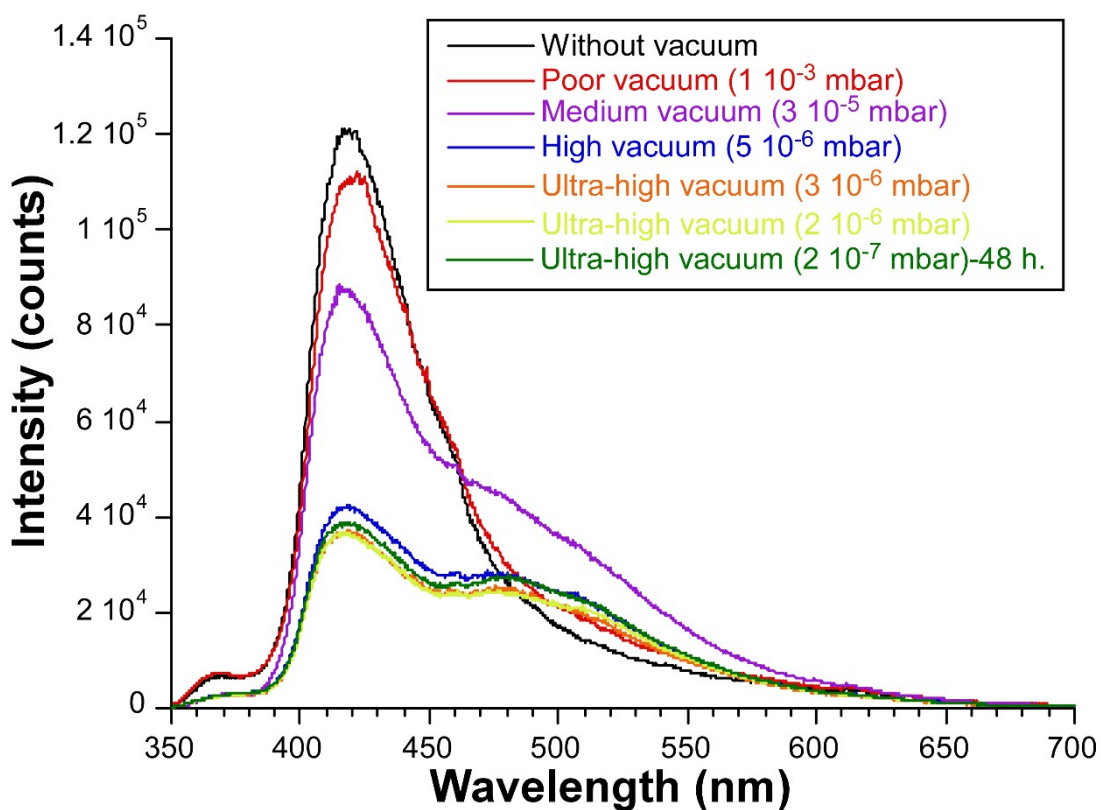


Figure S15. Evolution of the emission spectrum of the membrane **1@PMMA** recorded at RT under variable vacuum.

Once the membrane is under high vacuum, the reversibility of the vacuum-induced response has been also monitored by slowly breaking the vacuum in the cryostat containing the sample and recording an emission spectrum with the same setup. As observed in the figure below, as the vacuum is lost and room conditions at open atmosphere are restored, the emission spectrum recovers its initial shape by losing the band peaking at $\lambda_{em} = 480$ nm.

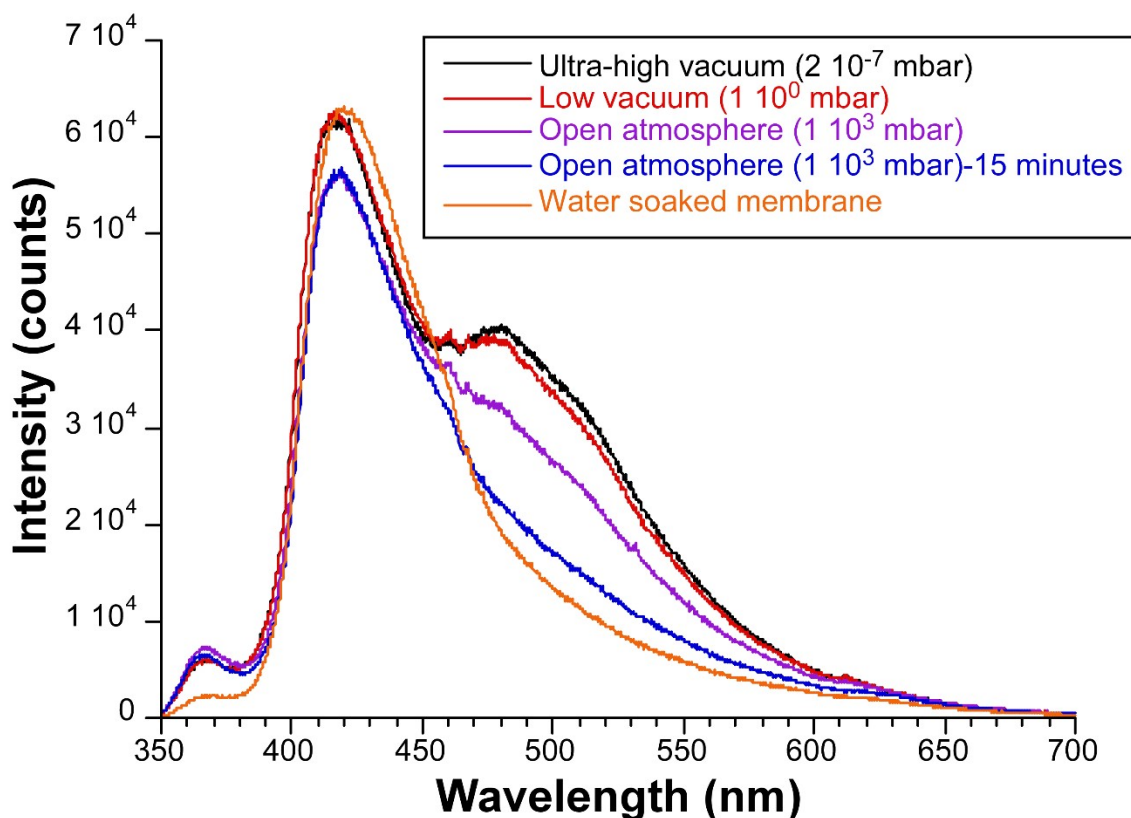


Figure S16. Evolution of the emission spectrum of the membrane **1@PMMA** recorded at RT under variable vacuum.

The thermometric analysis has been repeated in the low temperature region (10–310 K) for the **1@PMMA** membrane given that the hybrid keeps the vacuum-induced response. The same methodology followed to decompose the bands in energy scale has been applied to analyse the spectra given the structured shape of the bands in the membrane.

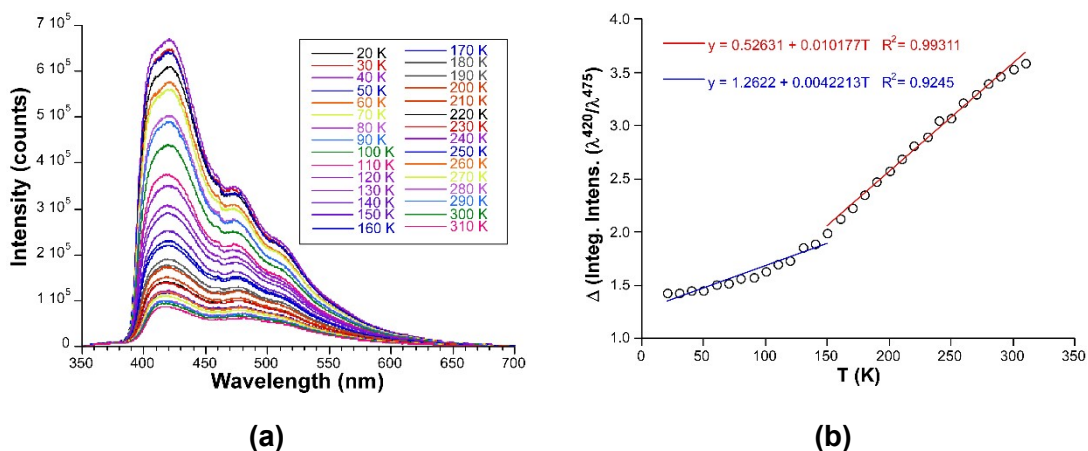


Figure S17. Thermometric activity of the **1@PMMA** membrane in the low-temperature range showing (a) the evolution of the emission spectra and (b) the ratiometric signal dependence with temperature.

S12. Sensing in membranes.

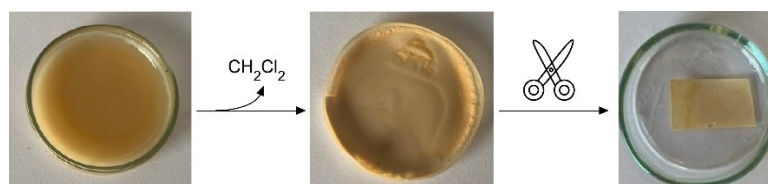


Figure S18. Schematic representation of the membrane formation showing the suspension in dichloromethane (left), after solvent evaporation (middle) and the cut section to be employed in sensing experiments (right).

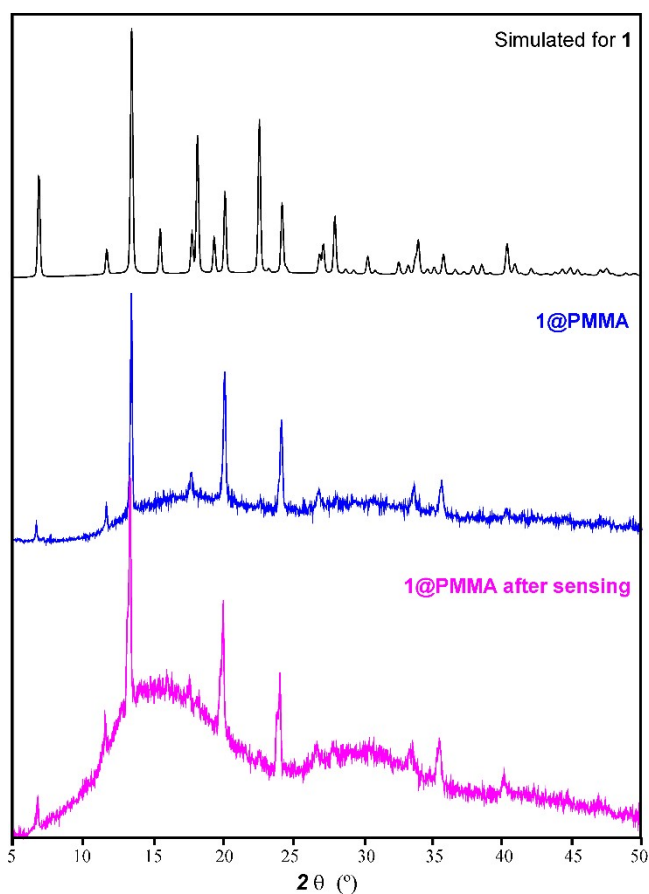
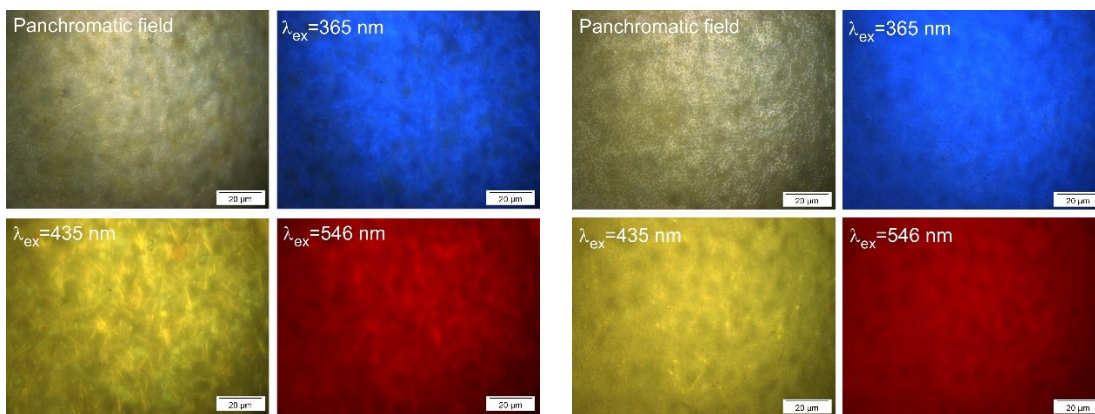


Figure S19. Comparison between the diffraction pattern of compound 1 and 1@PMMA before and after sensing experiments.

After sensing experiments, the main diffraction peaks assigned to compound 1 remain unaltered since there are no significant changes in terms of position, as well as is there any widening of the main peaks. Nonetheless, an increase in the bump is observed after sensing experiments, probably due to the mechanical stress suffered by the PMMA membrane during sensing measurements.



(a) **(b)**
Figure S20. Micro-photoluminescence images taken on the microscope over the two sides of the **1@PMMA** film.

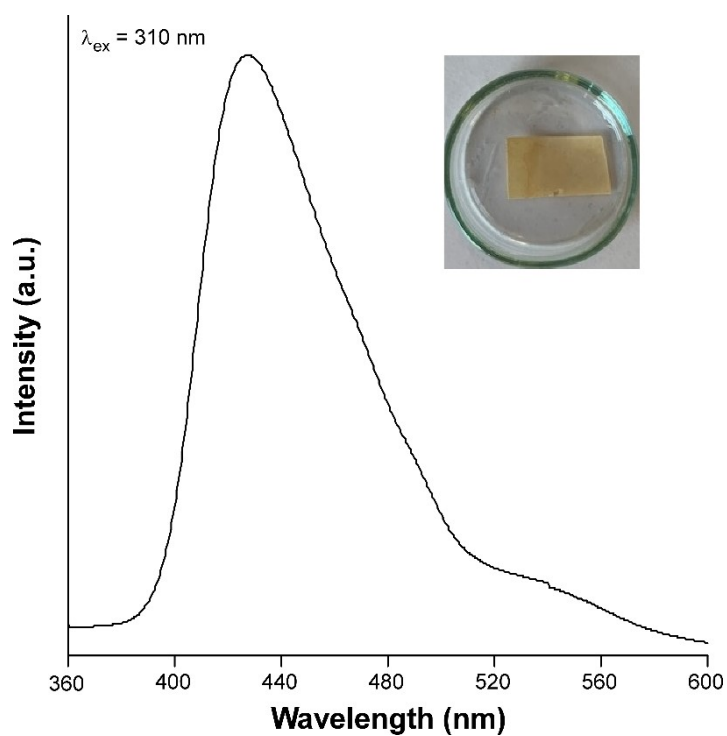


Figure S21. Emission spectrum taken on dry **1@PMMA** at room temperature being excited at 310 nm.

In view of the strong relationship between the applied vacuum and PL of the compound, a similar study was conducted for the **1@PMMA** membrane to check whether the behaviour is reproduced in these conditions. As shown in the next figure, a second band peaking at 480 nm becomes progressively more intense as the membrane is left under high vacuum for some hours.

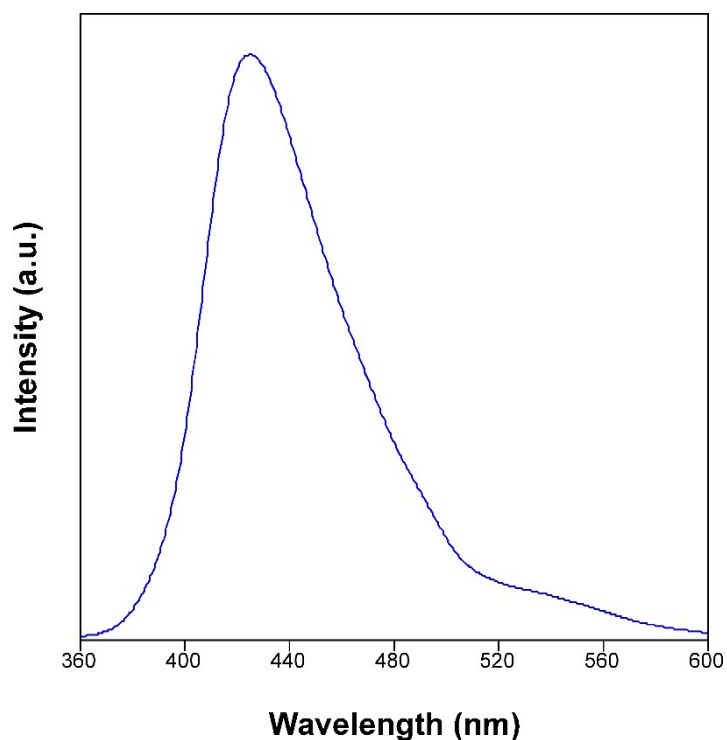


Figure S22. Emission spectrum of **1@PMMA** immersed in water at room temperature being excited at 310 nm.

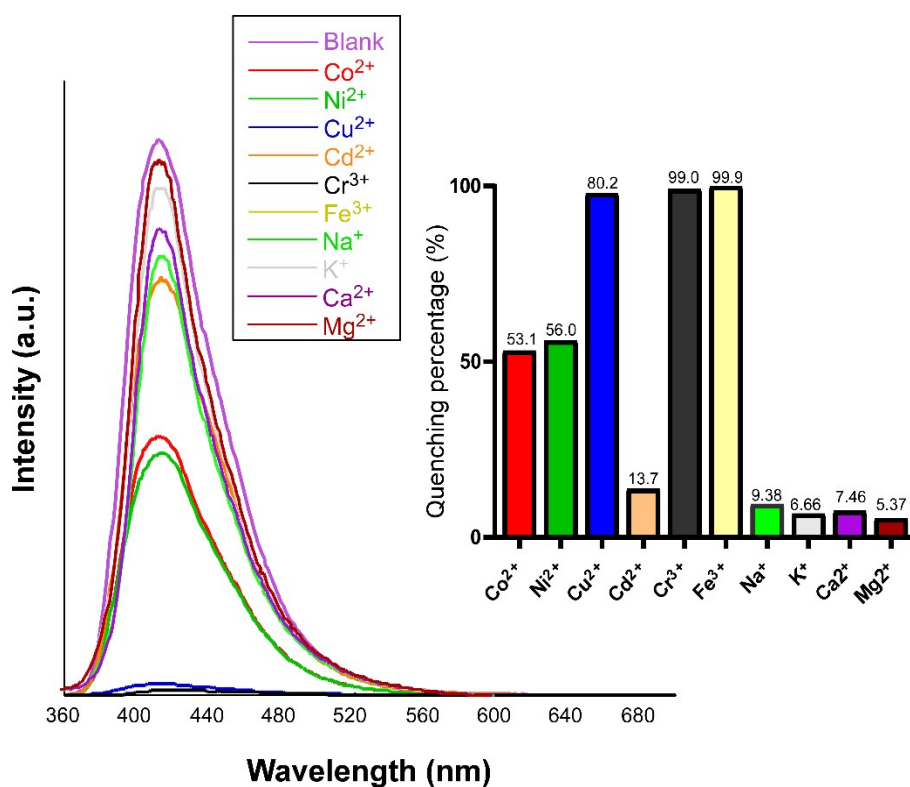


Figure S23. Emission spectra of **1@PMMA** soaked in different aqueous solutions of transition metals, alkaline and alkaline-earth ions with the quenching percentage of the photoluminescent signal ($\lambda_{\text{ex}} = 310$).

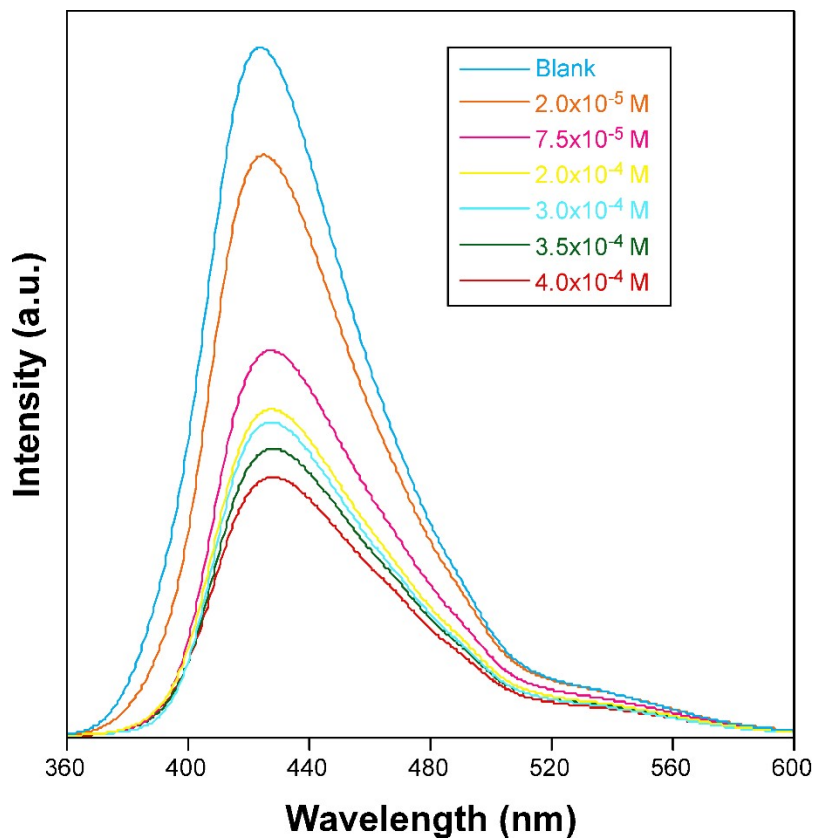


Figure S24. Emission spectra of **1@PMMA** under different concentration of Fe^{3+} ions in water ($\lambda_{\text{ex}} = 310$).

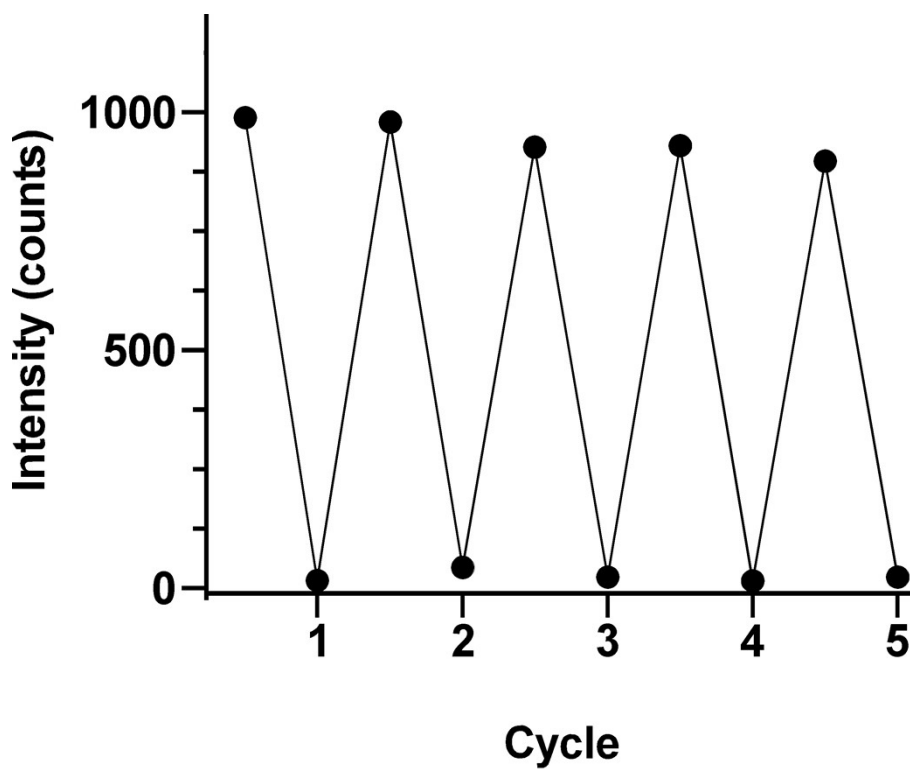


Figure S25. Emission intensity of **1@PMMA** upon successive washing and immersion in Fe^{3+} solution during five consecutive cycles ($\lambda_{\text{ex}} = 310$).

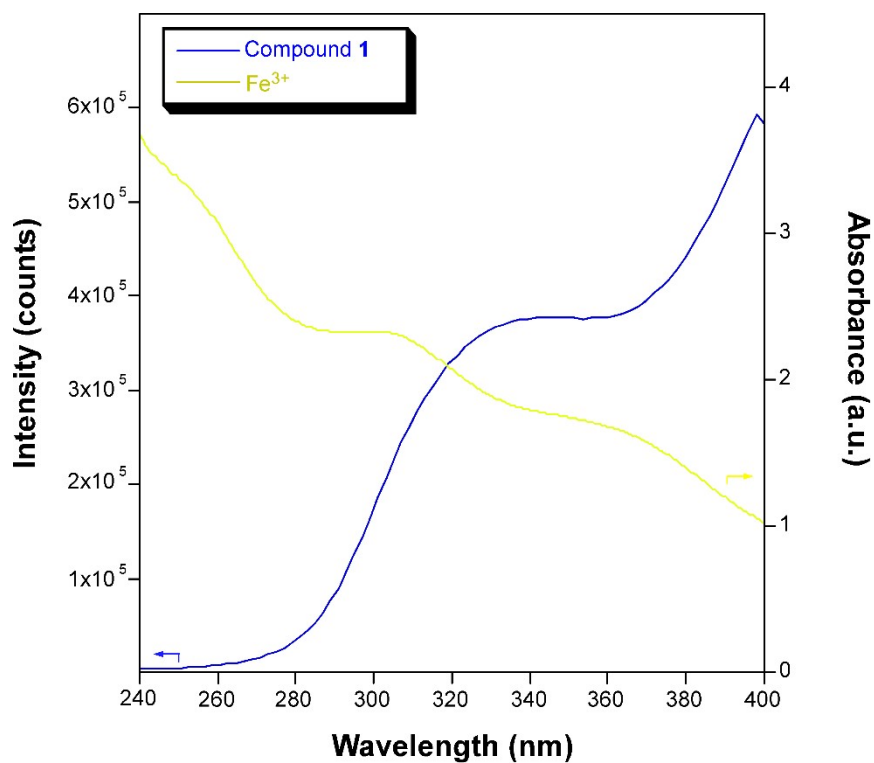


Figure S26. Simultaneous representation of absorbance spectrum of Fe^{3+} aqueous solution (yellow) and excitation spectrum of compound **1** ($\lambda_{\text{em}} = 430 \text{ nm}$) (blue).

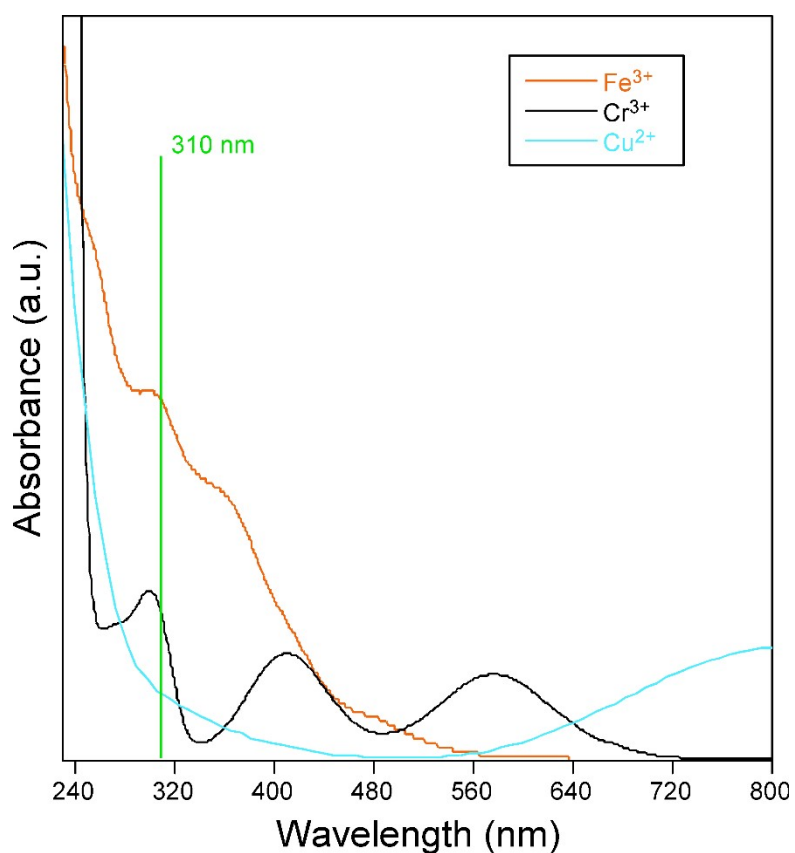


Figure S27. UV-vis absorption spectra of $1 \times 10^{-3} \text{ M}$ solution of Fe^{3+} , Cr^{3+} and Cu^{2+} . The green line indicates excitation wavelengths for monitoring sensing activity.

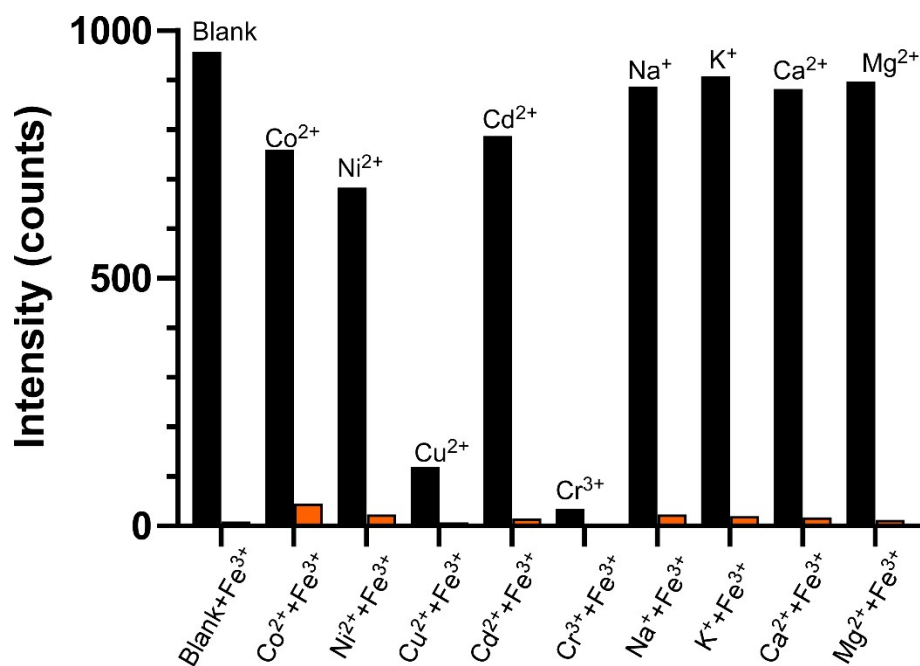


Figure S28. Quenching efficiency of Fe³⁺ towards **1@PMMA** in the presence of interferent ions.

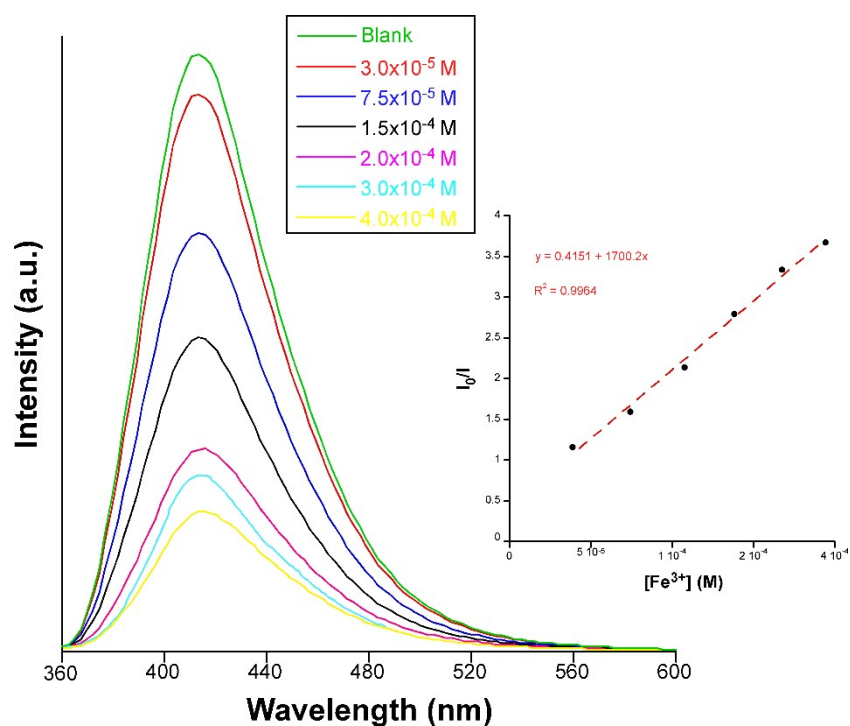


Figure S29. Emission spectra of **1@PMMA** toward varying Fe³⁺ concentration using tap water ($\lambda_{\text{ex}} = 310 \text{ nm}$). The inset shows the Stern-Volmer plot.

Table S7. A comparison of the Stern-Volmer constant (K_{SV}) and limit of detection (LOD) of MOFs toward Fe^{3+} sensing.

Compound	K_{SV} (M^{-1})	LOD (μM)	Medium	Ref.
$\{[Cu_2(ttpa)_2][Cu(BPTC)] \cdot 3H_2O \cdot DMF\}_n$	3.82×10^3	2.59	H ₂ O	15
$[Zn(tba)_2] \cdot DMA$	4.85×10^4	0.84	DMF	16
$[Zn_2(tpcb)(bpdc)_2]_n$	1.33×10^4	0.88	H ₂ O	17
$[ZnL(Bipy)] \cdot 0.5H_2O$	7.83×10^3	-	H ₂ O	18
$\{[Cd_3(itp)_2(btc)_2] \cdot 4H_2O\}_n$	5.88×10^4	0.12	EtOH	19
$\{[Cd(bmima)_{0.5}(atp)(H_2O)] \cdot DMF \cdot 0.5H_2O\}_n$	3.16×10^4	1.92	H ₂ O	20
Eu ³⁺ @MIL-53-COOH(Al)	5.12×10^3	0.5	H ₂ O	21
$\{Tb(L)(BPDC)_{0.5}(NO_3)] \cdot H_3O\}_n$	4.30×10^4	-	DMF	22
$\{[Tb(tcmb)(H_2O)_2] \cdot 2H_2O\}_n$	1.49×10^4	0.67	H ₂ O	23
$[Tb_2(L)_3] \cdot 2H_2O$	7.73×10^3	0.78	H ₂ O	24
Eu-MOF@TOCNF	7.92×10^3	-	H ₂ O	25
Eu-MOF@ALD-PPS	4.36×10^3	-	DMF	26
EuL3	4.10×10^3	-	H ₂ O	27
SUMOF7II	2.10×10^4	26.6	H ₂ O	28
CALIX@UiO-66-NH ₂	2.32×10^3	6.74	H ₂ O	29
1@PMMA	3.7×10^3	2.8	H ₂ O	This work

S13. Scanning electron microscopy.

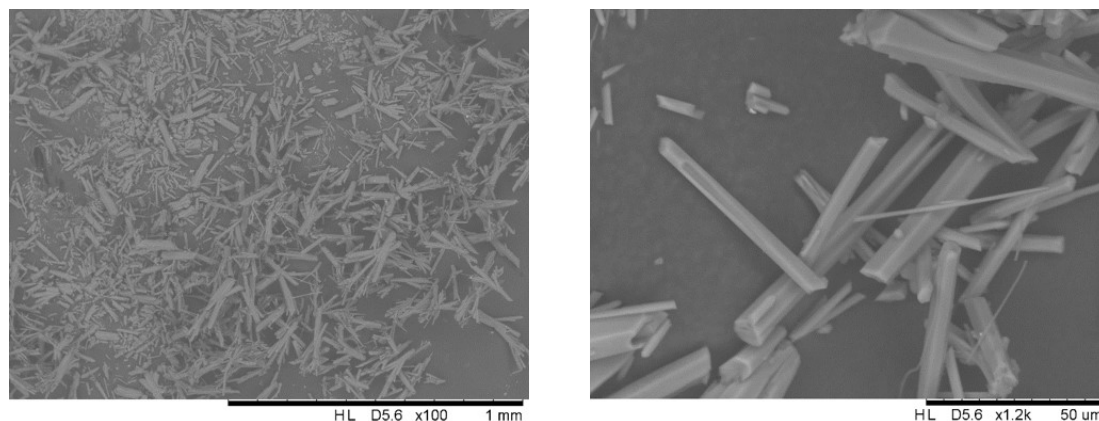


Figure S30. SEM images of a fresh sample of compound **1** showing the rod-like morphology of the crystals.

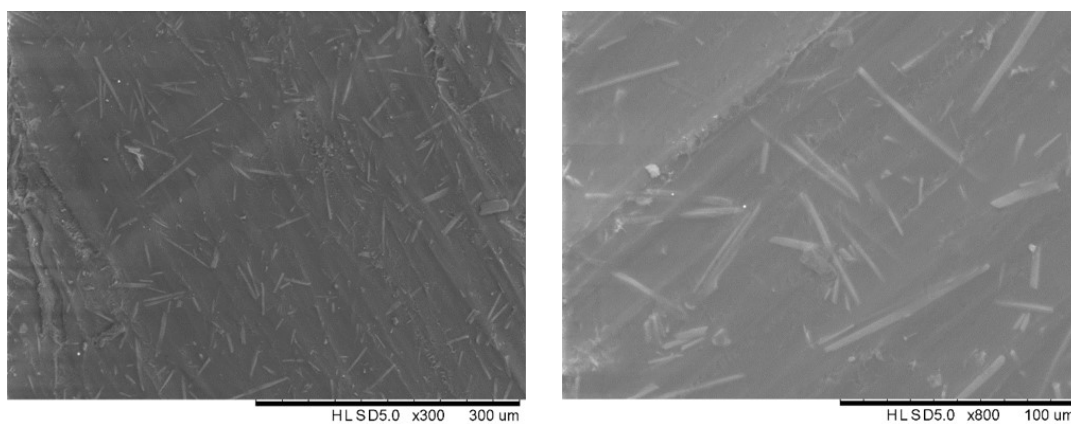


Figure S31. SEM images of **1@PMMA** showing the dispersion of the crystals of compound **1** in the membrane.

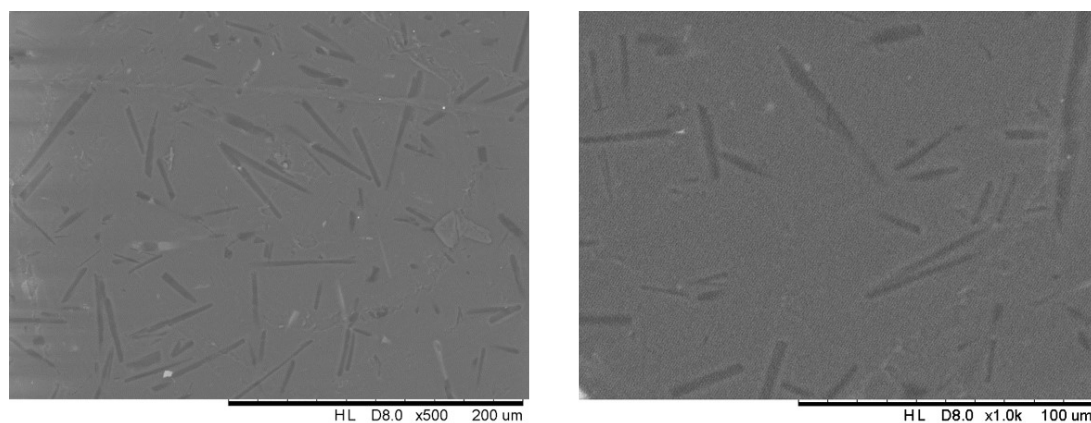


Figure S32. SEM images of **1@PMMA** after Fe³⁺ sensing experiments.

S14. References.

- 1 Bruker, *APEX2*, Madison, Wisconsin, USA, 2012.
- 2 G. M. Sheldrick, *SADABS, Empirical Absorption Correction Program*, 1997.
- 3 M. C. Burla, R. Caliandro, M. Camalli, B. Carrozzini, G. L. Casciarano, C. Giacovazzo, M. Mallamo, A. Mazzone, G. Polidori and R. Spagna, *J. Appl. Crystallogr.*, 2012, **45**, 357–361.
- 4 O. V. Dolomanov, L. J. Bourhis, R. J. Gildea, J. A. K. Howard and H. Puschmann, *J. Appl. Crystallogr.*, 2009, **42**, 339–341.
- 5 S. Inowlocki, *When Aseneth Met JosephKraemerRoss Shepard When Aseneth Met Joseph Oxford University PressNew York/Oxford*, 1998 , 1999, vol. 50.
- 6 M. J. Frisch, G. W. Trucks, H. B. Schlegel, G. E. Scuseria, M. A. Robb, J. R. Cheeseman, G. Scalmani, V. Barone, G. A. Petersson, H. Nakatsuji, X. Li, M. Caricato, A. V. Marenich, J. Bloino, B. G. Janesko, R. Gomperts, B. Mennucci, H. P. Hratchian, J. V. Ortiz, A. F. Izmaylov, J. L. Sonnenberg, D. Williams-Young, F. Ding, F. Lipparini, F. Egidi, J. Goings, B. Peng, A. Petrone, T. Henderson, D. Ranasinghe, V. G. Zakrzewski, J. Gao, N. Rega, G. Zheng, W. Liang, M. Hada, M. Ehara, K. Toyota, R. Fukuda, J. Hasegawa, M. Ishida, T. Nakajima, Y. Honda, O. Kitao, H. Nakai, T. Vreven, K. Throssell, J. A. Montgomery Jr., J. E. Peralta, F. Ogliaro, M. J. Bearpark, J. J. Heyd, E. N. Brothers, K. N. Kudin, V. N. Staroverov, T. A. Keith, R. Kobayashi, J. Normand, K. Raghavachari, A. P. Rendell, J. C. Burant, S. S. Iyengar, J. Tomasi, M. Cossi, J. M. Millam, M. Klene, C. Adamo, R. Cammi, J. W. Ochterski, R. L. Martin, K. Morokuma, O. Farkas, J. B. Foresman and D. J. Fox, *Gaussian 16, Revis. C.01, Gaussian Inc. Wallingford, UK, 2016*.
- 7 A. D. Becke, *J. Chem. Phys.*, 1993, **98**, 5648–5652.
- 8 B. Miehlich, A. Savin, H. Stoll and H. Preuss, *Chem. Phys. Lett.*, 1989, **157**, 200–206.
- 9 C. Lee, W. Yang and R. G. Parr, *Phys. Rev. B*, 1988, **37**, 785–789.
- 10 V. A. Rassolov, J. A. Pople, M. A. Ratner and T. L. Windus, *J. Chem. Phys.*, 1998, **109**, 1223–1229.
- 11 M. M. Francl, W. J. Pietro, W. J. Hehre, J. S. Binkley, M. S. Gordon, D. J. DeFrees and J. A. Pople, *J. Chem. Phys.*, 1982, **77**, 3654–3665.
- 12 P. J. Hay and W. R. Wadt, *J. Chem. Phys.*, 1985, **82**, 270–283.
- 13 N. M. O'Boyle, A. L. Tenderholt and K. M. Langner, *J. Comput. Chem.*, 2008, **29**, 839–845.
- 14 R. Dennington, T. A. Keith and J. M. Millam, *GaussView Version 6 2016*.
- 15 L. L. Qian, Z. X. Wang, J. G. Ding, H. X. Tian, K. Li, B. L. Li and H. Y. Li, *Dye. Pigment.*, 2020, **175**, 108159.
- 16 X. D. Fang, J. Yao, R. Fan, X. F. Bai, Y. E. Liu, C. F. Hou, Q. Q. Xu, A. X. Zhu and B. Huang, *J. Solid State Chem.*, 2021, **294**, 121854.
- 17 B. B. Rath and J. J. Vittal, *Inorg. Chem.*, 2020, **59**, 8818–8826.
- 18 D. Wang, D. Zhang, S. De Han, J. Pan, Z. Z. Xue, J. H. Li and G. M. Wang, *Dalt. Trans.*, 2019, **48**, 602–608.

- 19 T. R. Zheng, V. A. Blatov, Y. Q. Zhang, C. H. Yang, L. L. Qian, K. Li, B. L. Li and B. Wu, *J. Lumin.*, 2018, **199**, 126–132.
- 20 C. Li, X. Sun, X. Meng, D. Wang and C. Zheng, *CrystEngComm*, 2023, **25**, 2728–2738.
- 21 Y. Zhou, H. H. Chen and B. Yan, *J. Mater. Chem. A*, 2014, **2**, 13691–13697.
- 22 W. Yan, C. Zhang, S. Chen, L. Han and H. Zheng, *ACS Appl. Mater. Interfaces*, 2017, **9**, 1629–1634.
- 23 G. Tan, R. Q. Jia, W. L. Wu, B. Li and L. Y. Wang, *Cryst. Growth Des.*, 2022, **22**, 323–333.
- 24 C.-Y. Zhu, M.-T. Shen, H.-M. Cao, M.-J. Qi, P. Li, L. Chen, Y. Ge, W. Gao and X.-M. Zhang, *Microchem. J.*, 2023, **188**, 108442.
- 25 W. Wang, H. Cao, R. Fan, M. Zhu, R. Zhang and P. Liu, *Ind. Crops Prod.*, 2024, **222**, 119484.
- 26 W. Liu, H. Cui, J. Zhou, Z. Su, Y. Zhang, X. Chen and E. Yue, *ACS Omega*, 2023, **8**, 24635–24643.
- 27 M. Zheng, H. Tan, Z. Xie, L. Zhang, X. Jing and Z. Sun, *ACS Appl. Mater. Interfaces*, 2013, **5**, 1078–1083.
- 28 H. N. Abdelhamid, A. Bermejo-Gómez, B. Martín-Matute and X. Zou, *Microchim. Acta*, 2017, **184**, 3363–3371.
- 29 J. D. S. Fonseca, O. M. M. M. da Costa, S. Alves Júnior, B. S. Barros and J. Kulesza, *J. Braz. Chem. Soc.*, 2025, 36.